Brittle failure of β- and τ-boron: Amorphization under high pressure

Qi An[1,2,*] and Sergey I. Morozov[3]
[1]*Department of Chemical and Materials Engineering, University of Nevada, Reno, Reno, Nevada 89557, USA*
[2]*Nevada Institute for Sustainability, University of Nevada, Reno, Reno, Nevada 89557, USA*
[3]*Department of Computer Simulation and Nanotechnology, South Ural State University, Chelyabinsk 454080, Russia*
(Received 9 October 2016; revised manuscript received 15 January 2017; published 17 February 2017)

Element boron tends to form an icosahedral motif involving 26 electrons, leading to intriguing bonding conditions which complicate understating the structural variations under high pressure. Here we used density function theory (DFT) to examine the mechanical response of β- and recent discovered τ-boron to shear along the most plausible slip system. We found that the failure mechanism of β-B_{106} is fracturing a B_{28} triply fused icosahedral cluster without destroying a regular B_{12} icosahedron, while the failure of τ-B_{106} arises from the disintegration of a B_{28} cluster and one nearby icosahedron. The failure of β-B_{106} leads to a B_{12}-embedded amorphous structure which transforms to the second amorphous phase with a fully deconstructed icosahedra at 81 GPa. The second amorphous phase retains the deconstructed icosahedra at ambient conditions which is different from the normal amorphous boron containing regular icosahedra which are bonded randomly to each other. The second amorphous phase is more stable than β-B_{106} above 90 GPa, which explains the previous experiments on pressure-induced amorphization. In addition, forming the second highest density amorphous phase likely causes the brittle failure of β-B and related materials.

DOI: 10.1103/PhysRevB.95.064108

I. INTRODUCTION

Elemental boron exhibits extreme chemical complexity which arises from the cagelike icosahedral motif involving 26 bonding electrons delocalized over the skeleton. This leads to at least 16 identified boron polymorphs [1]. However, only three pure boron phases are well characterized: α-B_{12} [1], β-B_{106} [2], and γ-B_{28} [3] with 12, 106, and 28 atoms in the unit cell, respectively, while others are stabilized by impurities or geometrical frustration [4]. Among these pure boron phases, γ-B_{28} is the most stable phase at high pressure above 19 GPa [3], while α-B_{12} and β-B_{106} are more stable at ambient conditions. However, there is a long debate about which phase is more stable between α-B_{12} and β-B_{106} at ambient conditions [5–7]. Recently, using high-resolution transmission electron microscopy (HRTEM) and DFT simulations, the β-boron powders were found to contain two different types of grains [8]: (1) the normal twins containing a number of randomly spaced twin planes; and (2) what appears to be a fully transformed twinlike structure. This fully transformed structure, denoted here as τ-B, is a new crystalline phase based on the *Cmcm* orthorhombic space group [8].

Boron and boron compounds exhibit such unique physical and chemical properties as superhard, high-temperature superconductivity, low density, high melting temperature, high abrasion resistance, and high resistance to radiation damage [9–15]. The combination of these properties makes them widely used as doping semiconductors, superconducting materials, reinforcing chemical additives, armor materials, nuclear energy materials, and refractory materials [11–17]. However, these boron based materials suffer from the brittle failure as other ceramics, which prevents them from extensively commercial applications. For example, boron carbide (B_4C) experiences unusually brittle failure under hypervelocity impact [16,18]. Because of the complex structure-property relationships in the boron phases, little advance has been made in understanding their brittle failure which is essential to interpreting their mechanical behaviors under high pressure.

Searching possible superconducting phases of low-Z elements under high pressure is of great interest because their high Debye temperature might increase the superconductivity transition temperature [19]. Eremets *et al.* [19] reported that β-B_{106} transforms from a nonmetal to a superconductor above 170 GPa at 6 K. A crucial and open question related to this phenomenon is what is the structure related to the superconductivity mechanism? In particular, whether the icosahedral clusters exist or not at the superconductivity transition pressure [20]? Sanz *et al.* [21] reported the phase transformation of crystalline β-B_{106} to an amorphous phase over 100 GPa, suggesting that the superconducting phase may be related to the amorphous phase. Using DFT, Häussermann *et al.* [22] investigated various crystalline boron phases at high pressures and found that the α-Ga boron crystalline phase is more stable than α- and β-boron above 74 GPa. Thus, α-Ga boron might be a candidate for the superconducting phase [22]. However, the x-ray diffraction analysis on the compressed β-B_{106} showed the amorphization of β-B_{106} at $\sim$100 GPa [21], indicating the existence of metastable amorphous phases. A recent DFT study showed the amorphization of β-B above 200 GPa [23], but the transition pressure is much higher than the experimental observation [21].

In this work we used DFT to examine the deformation and intrinsic failure mechanism of β-B, τ-B_{106}, and α-B_{12} shearing along the most plausible slip system. We found that the B_{12} icosahedron has better resistance to shear than the B_{28} triply fused icosahedral cluster in β- and τ-B, leading to forming an amorphous structure composed of deconstructed B_{28} clusters and regular B_{12} icosahedra. As this amorphous phase is compressed to high pressure above 81 GPa, it transforms to the second amorphous phase with fully destroyed

*Corresponding author: qia@unr.edu

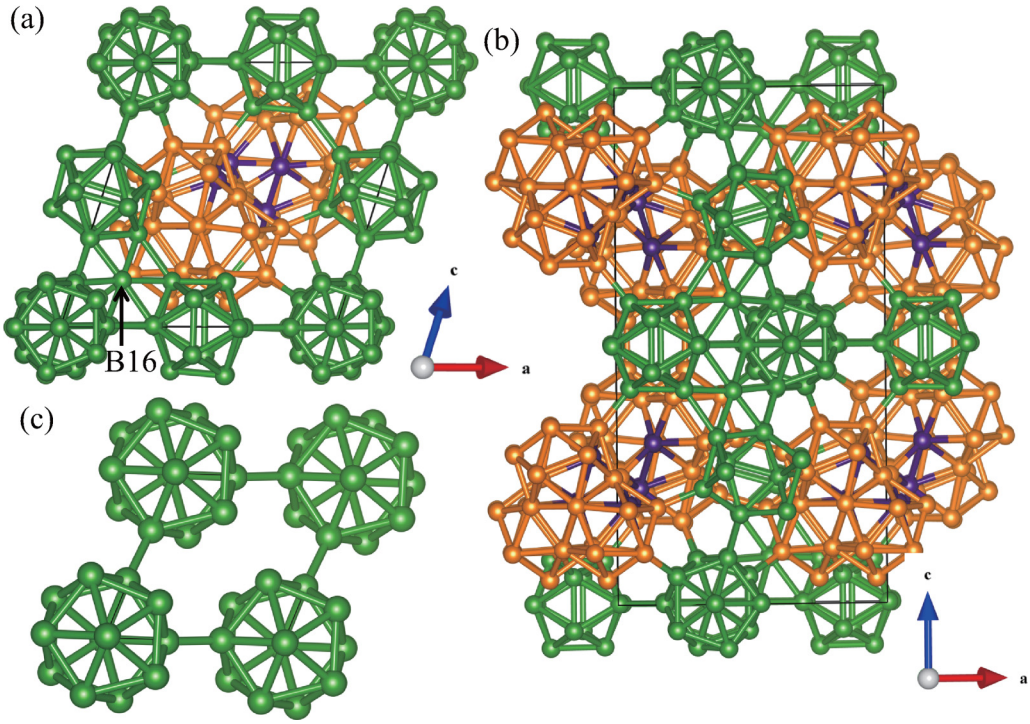

FIG. 1. Structure of various B phases: (a) Structure of β-B_{105} with B16 POS, (b) structure of τ-B_{106}, and (c) structure of α-B_{12}. The B_{12} icosahedra and the B_{28} units are represented by green and orange balls, respectively. The B13 site is represented by the purple balls.

B_{12} icosahedra. The second amorphous phase is more stable than crystalline β-B_{106} above 90 GPa, which explains the experimental observed amorphization of β-B. In addition, the connection between amorphous phase formation and brittle failure is discussed.

II. COMPUTATIONAL METHODS

All simulations were performed used the Vienna *ab initio* simulation package (VASP) periodic code with plane wave basis sets [24–27]. The Perdew-Burke-Ernzerhof (PBE) functional is used accounting for the exchange-correlation and the projector augmented wave method is applied to account for the core-valence interaction. An energy cutoff of 600 eV is used in all the simulations since it gives excellent convergence on energy, force, stress, and geometries. The energy error for terminating the electronic self-consistent field (SCF) and the force criterion for the geometry optimization were set equal to 10^{-6} eV and 10^{-3} eV/Å, respectively. Reciprocal space was sampled using the Γ-centered Monkhorst-Pack scheme with a fine resolution of $2\pi \times 1/40$ Å^{-1} for all calculations except for the shear deformation.

The elastic constants C_{ij} were calculated from the stress-strain relationship as a function of various cell distortions from the equilibrium lattice configuration [28]. The elastic constants will be presented to one hundredth of a GPa since the stress uncertainty arising from the force converge criterion is less than 0.16 GPa. To examine shear deformation, we imposed the strain for a particular shear plane while allowing full structure relaxation for the other five strain components [29]. A 1% level of strain was predefined as the small strain increment for each deformation step. The stress is defined as the force per deformed area, and the strain is defined as the true strain. The Monkhorst-Pack grid ($2\times2\times2$) in the k space was used in the shear deformation.

III. RESULTS AND DISCUSSION

A. Crystal structure of α-B_{12}, β-B, and τ-B_{106}

The β-B structure was first proposed by Hoard and denoted as β-B_{105} [30] which consists of 105 atoms with 15 nonequivalent boron positions (B1 to B15) in the rhombohedral unit cell. Figure 1(a) showed the unit cell where four icosahedra are located at the vertex sites and edge centers and one single atom (B15) is located in the cell center connecting to two B_{28} triply fused icosahedral clusters through the B13 sites. Later, the β-B_{105} structure was refined experimentally [31] and theoretically [6] to be β-B_{106} with partially occupied sites (POS) and 106 atoms in the unit cell. Furthermore, lower energy structures were proposed and verified by QM simulations considering other POS sites B17–B20 [32,33]. To considerer the most abundant POS in the β-B, we selected one particular β-B_{106} structure with one B13 vacancy and two B16 POS [6]. We will examine both β-B_{106} and β-B_{105} structures to illustrate how the POS affect such mechanical properties as bulk modulus, shear modulus, hardness, and failure mechanism. We will also examine the new identified τ-B_{106} phase that can be thought of as a perfectly ordered twinlike version of the original β-B_{106} structure [8], as shown in Fig. 1(b).

Phase α-B_{12} has a relative simple crystalline structure with only one icosahedron located at the vertex of the rhombohedral

unit cell, as displayed in Fig. 1(c). In α-B_{12} each icosahedron is connected to 12 nearby icosahedra through six two-center–two-electron (2c–2e) bonds and six three-center–two-electron (3c–2e) bonds. As a result each icosahedron contributes $6 + 6\times2/3 = 10$ electrons for the intericosahedral bonds and leaving 26 electrons for 13 intraicosahedral bonds (Wade's rule [34]).

B. Elastic properties of α-B_{12}, β-B_{105}, β-B_{106}, and τ-B_{106}

To establish the structure-property relationship of these boron phases, we first computed the elastic properties including elastic moduli, bulk modulus, and shear modulus. The predicted elastic moduli for α-B_{12}, β-B_{105}, β-B_{106}, and τ-B_{106} are listed in Tables S1−S4 of the Supplemental Material (SM) [35], respectively. This leads to a calculated bulk modulus $B = 202.5$ GPa and shear modulus $G = 189.1$ GPa for τ-B_{106} using Voigt-Reuss-Hill averaging [36]. In contrast, the predicted $B = 204.2$ GPa and $G = 196.7$ GPa for β-B_{106}, which agree very well with previous experiments [21,37] and theoretical prediction [23,33]. Thus, the bulk and shear modulus of β-B_{106} is slightly higher than τ-B_{106}. For the defect-free β-B_{105} phase the computed $B = 197.2$ GPa and $G = 185.6$ GPa which are lower than those of β-B_{106}, indicating that the POS in β-B_{106} increase the B and G by 3.6% and 6.0%, respectively. For the α-B_{12} phase, the computed $B = 211.7$ GPa and $G = 200.8$ GPa, which are consistent with previous experiment [38] and theoretical prediction [39]. The α-B_{12} phase has the largest bulk modulus and shear modulus among these four phases. The calculated bulk modulus and shear modulus are listed in Table I.

It is well known that the Voigt-Reuss-Hill approach combines the upper (Voigt) and lower (Reuss) bounds for the polycrystalline moduli. To estimate the uncertainty of our calculations, the Voigt, Reuss, and Hill moduli are listed in Table S5 of the SM [35]. The differences of Voigt and Reuss moduli for β-B_{105}, β-B_{106}, and τ-B_{106} are within 0.2%, while for α-B_{12} they increase to 4.1% and 0.4% for the shear modulus and bulk modulus, respectively.

Indentation hardness measures the resistance of materials to deformation due to a constant compressive load and is related to materials strength. To compare the hardness of these four phases, we calculated the Vickers hardness (H_v) for polycrystalline materials based on G/B [40] that leads to $H_v =$ 39.1, 38.3, 36.6, and 38.8 GPa for β-B_{106}, τ-B_{106}, β-B_{105}, and α-B_{12}, respectively (Table I). Thus, the sequence from high to low hardness is β-$B_{106} > \tau$-$B_{106} > \alpha$-$B_{12} > \beta$-B_{105}. Thus, the β-B_{106} is slightly stronger than τ-B_{106}. This also suggests that the presence of twins in β-B_{106} will slightly soften the materials since τ-B_{106} is the regular twinned phase of β-B_{106}. The hardness of β-B_{106} is larger than that of β-B_{105} by 6.3%, indicating that the POS in β-B_{106} makes it stronger than defect-free β-B_{105}.

TABLE I. Bulk modulus, shear modulus, hardness, and ideal shear stress for α-B_{12}, β-B_{105}, β-B_{106}, and τ-B_{106}.

Structure	α-B_{12}	β-B_{105}	β-B_{106}	τ-B_{106}
Bulk modulus (GPa)	211.7	197.2	204.2	202.5
Shear modulus (GPa)	200.8	185.6	196.7	189.1
Theoretical Vickers hardness (GPa)	38.8	36.6	39.1	38.3
Ideal shear stress (GPa)	28.5	29.5	33.1	31.7

C. Shear deformation and failure mechanism of α-B_{12}, β-B_{105}, β-B_{106}, and τ-B_{106}

To determine the deformation and failure mechanism of the β-B_{106}, τ-B_{106}, β-B_{105}, and α-B_{12}, we applied pure shear deformation on these four phases. Previous experiments [41] and theoretical studies [42] showed that the most plausible slip plane for boron carbide (B_4C) is $\{001\}_r$ plane. Here we used subscript "r" to represent the planes and directions in the rhombohedral cell. The B_4C is a modification of α-B_{12} where the C-B-C chain is inserted among icosahedra [42]. Thus, we considered the most plausible slip plane for α-B_{12} to be the $\{001\}_r$ plane. For β-B_{106}, the most abundant twin plane observed in experiments is $\{001\}_r$ [4,43], which is exactly the same as B_4C and B_6O [44,45]. This suggests that the most plausible slip plane for β-B_{106} is $\{001\}_r$ which is the same as B_4C and B_6O [44,45]. After the slip plane is identified, we determined the easiest slip direction by applying shear deformation along $\langle 100\rangle_r$ and $\langle \bar{1}00\rangle_r$ directions in $\{001\}_r$ plane for α-B_{12} and β-B_{106}. The ideal shear stresses for α-B_{12} and β-B_{106} shearing along $\langle \bar{1}00\rangle_r$ direction are 28.5 and 33.1 GPa which are lower than those shearing along the opposite $\langle 100\rangle_r$ direction, as shown in Fig. S1 of the SM [35]. Thus, the most plausible slip system for α-B_{12}, β-B_{106}, and β-B_{105} is $\{001\}_r/\langle \bar{1}00\rangle_r$. For τ-B_{106} it was sheared along the twin plane which corresponds to the slip system of $\{001\}_r/\langle \bar{1}00\rangle_r$ in β-B_{106}.

The stress-strain relationships for α-B_{12}, β-B_{105}, β-B_{106}, and τ-B_{106} are displayed in Fig. 2. In the elastic region (<0.08 shear strain) the slope of the stress-strain curve for α-B_{12} is larger than the other three phases, which is consistent with the above prediction that α-B_{12} has the largest shear modulus. The ideal shear strengths listed in Table I are

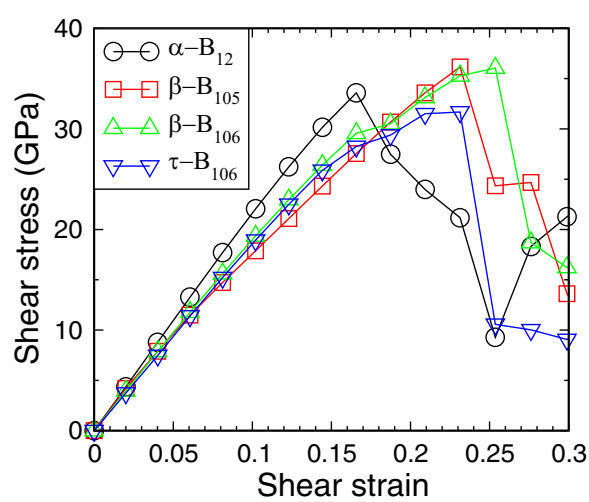

FIG. 2. Stress-strain relationships for α-B_{12}, β-B_{105}, β-B_{106}, and τ-B_{106} shearing along the most plausible slip system.

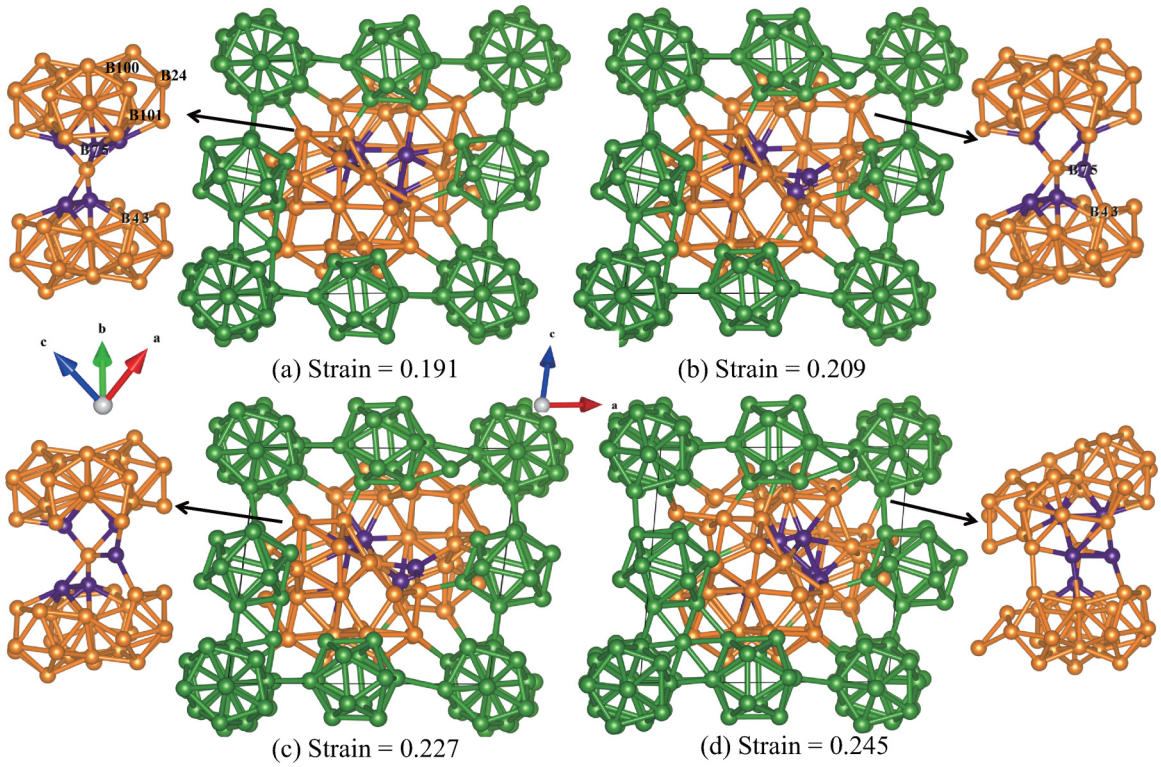

FIG. 3. Failure mechanism of β-B_{106} shearing along the $(001)_r/\langle 100\rangle_r$ slip system: (a) Structure at 0.191 strain where the β-B_{106} deforms elastically, (b) structure at 0.209 strain where the B75 atom in the B_{28} cluster is displaced and bonded to the B43 atom, (c) structure at 0.227 strain before failure, and (d) failure structure at 0.245 strain showing the deconstruction of only B_{28} clusters.

28.5, 29.5, 33.1, and 31.7 GPa for α-B_{12}, β-B_{105}, β-B_{106}, and τ-B_{106} phases, respectively. Comparing the ideal shear stress for these four structures, the sequence from high to low strength is β-$B_{106} > \tau$-$B_{106} > \beta$-$B_{105} > \alpha$-B_{12}. Thus, the POS in β-B_{106} increase the strength and stabilize the defect-free β-B_{105} structure, while the twins decrease the strength. This strength sequence for a perfect crystal is consistent with the above Vickers hardness prediction on the polycrystalline materials. To understand these behaviors, we discussed the detailed deformation and failure mechanisms as follows.

We first examined the deformation mechanism of β-B_{106} shown in Fig. 3. As we sheared the intact structure to 0.191 strain, it deforms elastically without breaking any bonds as shown in Fig. 3(a). The most stretched bonds are B24–B100 and B24–B101 that increase from the original 1.86 and 1.84 Å to 2.04 and 2.03 Å, respectively. With the shear strain increasing to 0.207, the B75 atom connecting to the center atom is displaced and bonded to the B43 atom in the opposite B_{28} cluster, as shown in Fig. 3(b). This slightly releases the shear stress from 31.5 GPa at 0.191 strain to 31.4 GPa at 0.207 strain. As the shear strain continuously increases to 0.227 corresponding to the maximum shear stress of 33.1 GPa, neither B_{12} icosahedra nor B_{28} clusters are deconstructed as displayed in Fig. 3(c). After passing the critical strain of 0.227, the B_{28} clusters are disintegrated as shown in Fig. 3(d), leading to the failure of β-B_{106}. However, no B_{12} icosahedron is disintegrated in this failure process, indicating that the B_{12} icosahedron has better resistance to shear than the B_{28} cluster.

Then we investigated the deformation and failure mechanism of τ-B_{106} which also helps understand how the twins in β-B_{106} affect the failure mechanism. Figure 4 displayed the structural changes at various critical strains. The intact structure is shown in Fig. 4(a). As the shear strain increases to 0.209, no bond breaks as shown in Fig. 4(b). The most stretched bonds are B128–B204 and B128–B205 that increase from the original 1.84 and 1.85 Å to 2.11 and 2.15 Å, respectively. With the shear strain increasing to 0.231 which corresponds to the maximum shear stress of 31.7 GPa, these two bonds break and the B128 atom is bonded to the nearby icosahedron within the twin plan. But the B_{28} clusters are not deconstructed, as shown in Fig. 4(c). After passing the critical strain of 0.231, the B_{28} cluster is deconstructed, leading to the disintegration of the B_{12} icosahedron within the twin plane, as shown in Fig. 4(d). In contrast to the fractural failure of β-B_{106}, the displaced atom in the B_{28} cluster interacts with the B_{12} icosahedron within the twin plane, leading to their deconstruction and failure of τ-B_{106}. The twins destabilize the β-B_{106} crystal structure and it changes the deformation mechanism, leading to lower shear stress for τ-B_{106}. It is interesting to notice that only one B_{12} icosahedron within the twin plane is deconstructed while the other seven are not fractured, indicating that the B_{12} icosahedron has better shear resistance than the B_{28} cluster.

To examine how the POS affect the failure mechanism in β-B, we sheared the β-B_{105} as displayed in Fig. 5. When it was sheared to 0.191 strain corresponding to the maximum shear stress of 29.5 GPa, the B_{28} cluster is stretched without breaking

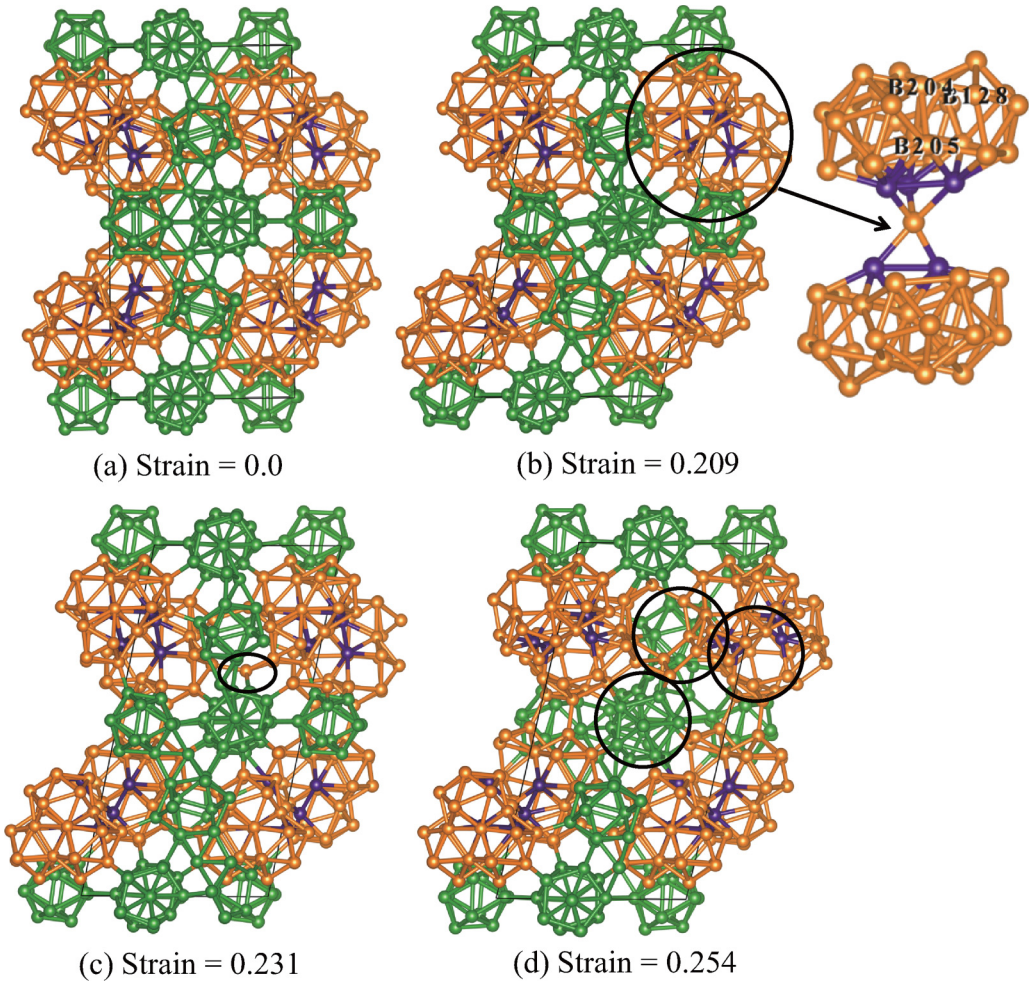

FIG. 4. Failure mechanism of τ-B_{106} under shear deformation along $\{001\}_r$ twin plane: (a) Unstrained structure, (b) structure at 0.209 strain, (c) structure before failure (0.231 strain) where the atom in the B_{28} unit bonds to the B_{12} icosahedron leading to the plastic deformation, and (e) structure at 0.254 strain after failure. The failure arises from the interaction of B_{28} and B_{12} icosahedron units, which is shown in the oval regions. The B_{12} icosahedra and B_{28}-B-B_{28} units are represented by green and orange balls, respectively. The B13 site is represented by the purple balls.

any bonds, as shown in Fig. 5(a). The most stretched bonds are B24–B100 and B24–B101 that increase from 1.86 and 1.84 Å to 2.12 and 2.06 Å, respectively. As the shear strain increases to 0.209, one of three fused icosahedra in the B_{28} cluster is deconstructed as shown in Fig. 5(b). This releases the shear stress from 29.5 to 22.7 GPa. However, the other two fused icosahedra in the B_{28} cluster are not deconstructed. Therefore the shear stress continuously increases from 22.7 to 26.4 GPa as the shear strain increases from 0.209 to 0.263 without fracturing the whole B_{28} cluster, as shown in Fig. 5(c). With the shear strain further increasing to 0.280, the B_{28} cluster is fully deconstructed as shown in Fig. 5(d). Meanwhile one icosahedron in the edge center is also deconstructed, leading to the failure of β-B_{105}.

Finally we examine the deformation mechanism of α-B_{12} as displayed in Fig. 6. Figure 6 also shows the isosurface (at 0.85) of the electron localization function (ELF) [46] which enables an effective and reliable analysis of covalent bonding. Figure 6(a) displays the intact structure with two types of bonds: 2c–2e bond (such as B5–B79) and 3c–2e bond (such as B52–B54–B74). When the α-B_{12} is sheared to 0.117 strain where the plastic deformation starts, the 3c–2e is distorted close to the B52–B74 center and the B52–B74 distance decreases from the original 2.01 to 1.95 Å [Fig. 6(b)]. Meanwhile the B52–B54 distance increases from the original 2.01 to 2.40 Å, and the B54–B74 distance decreases from the original 2.01 to 1.97 Å. As the shear strain increases to 0.331 strain, the B52–B74 distance further decreases to 1.80 Å and the 3c–2e bond is even closer to B52–B74. At the same time the B5–B79 (2c–2e) bond increases from the original 1.67 to 1.74 Å [Fig. 6(c)]. After passing the critical strain of 0.331, both the B52–B54–B74 (3c—2e) and B5–B79 (2c–2e) bonds are broken, leading to formation of new B52–B74–B5 (3c–2e) and B6–B80 (2c–2e) bonds. This process releases the shear stress and the structure transforms back to α-B_{12} phase without fracturing the icosahedra, as shown in Fig. 6(d). This indicates that the B_{12} icosahedron has good resistance to shear deformation. In addition, α-B_{12} plastically deforms from 0.117

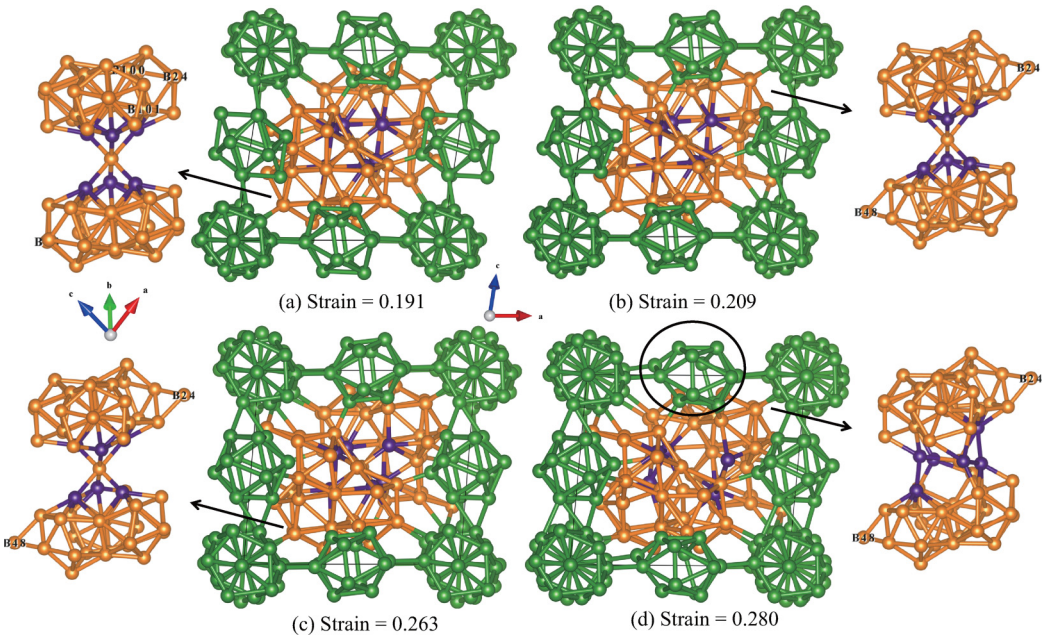

FIG. 5. Failure mechanism of β-B_{105} shearing along the $(001)_r/\langle\bar{1}00\rangle_r$ slip system: (a) Structure at 0.191 strain without broken bonds, (b) structure at 0.209 strain where one of the three fused icosahedra in the B_{28} cluster is deconstructed, (c) structure at 0.263 strain, and (d) structure at 0.280 with a fully deconstructed B_{28} cluster.

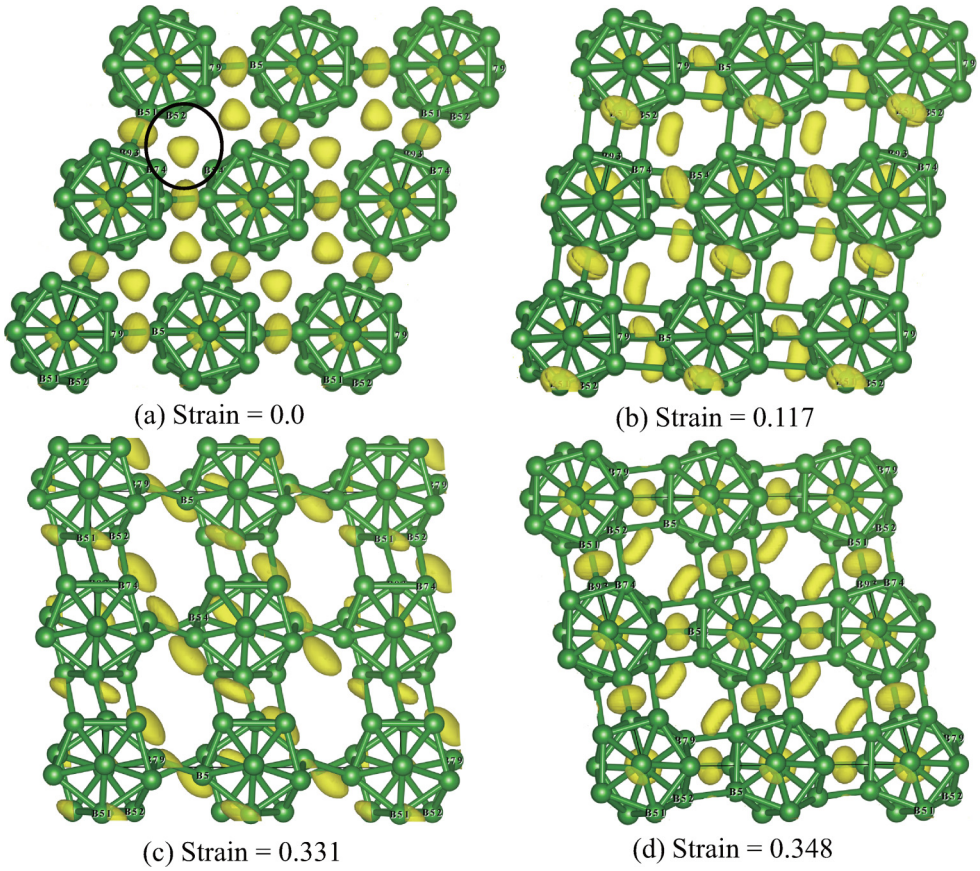

FIG. 6. Failure mechanism for α-B_{12} shearing along the $(001)_r/\langle\bar{1}00\rangle_r$ slip system: (a) Intact structure, (b) structure at 0.117 strain where plastic deformation starts, (c) structure at 0.331 before structural transformation, and (d) structure at 0.348 after structure transforming back to α-B_{12}.

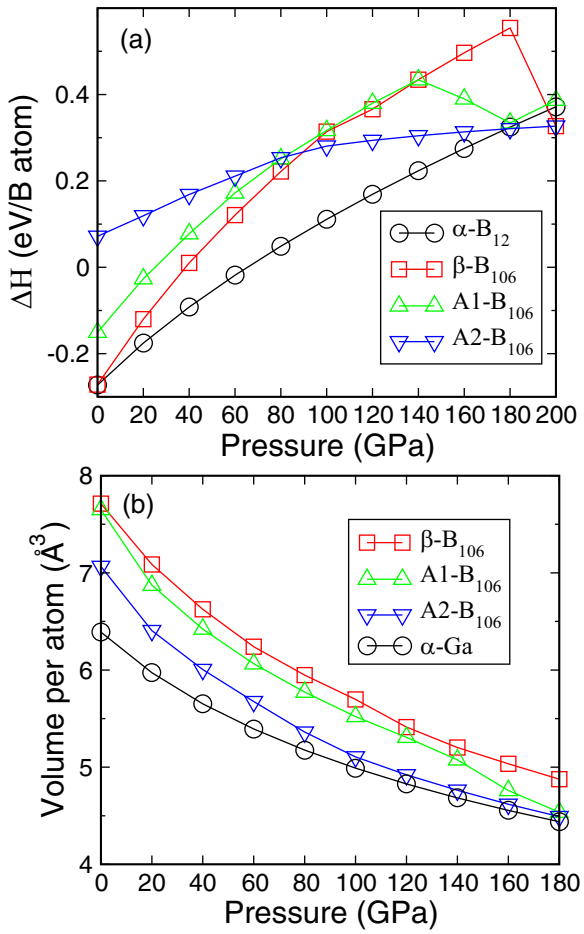

FIG. 7. (a) Enthalpy differences of α-B_{12}, β-B_{106}, amorphous phases A1-B_{106} and A2-B_{106} relative to α-Ga B phase as a function of pressure. (b) Atomic volume as a function of pressure predicted for α-Ga-B, β-B_{106}, A1-B_{106}, and A2-B_{106}.

to 0.331 strain due to the existence of 3c–2e bonds, which is much larger than the other three phases.

D. Amorphization of β-B_{106} under high pressure

To examine the amorphization of β-B_{106}, we compressed the crystalline β-B_{106} and shear induced amorphous structure (denoted as A1-B_{106}) to 200 GPa. Figure 7(a) displayed the enthalpy differences of α-B_{12}, β-B_{106}, and A1-B_{106} relative to high pressure α-Ga phase as a function of pressure. The crystalline β-B_{106} is stable up to 180 GPa and then the B_{28} cluster and B_{12} icosahedra are fully destroyed at 200 GPa to form the second amorphous structure denoted as A2-B_{106}. For the A1-B_{106}, the B_{12} icosahedra become unstable above 140 GPa and it continuously transforms to A2-B_{106} above 140 GPa, as indicated by the structural changes in Fig. S2 of the SM [35]. Therefore, shear lowers the amorphization pressure of β-B_{106}. To determine the phase boundaries of β-B_{106}, A1-B_{106}, and A2-B_{106}, we computed the (enthalpy, volume)-pressure relationships for A2-B_{106} and plotted them in Fig. 7. We found that the β-B_{106} will transform to the A2-B_{106} above 90 GPa, which agrees very well with experimental observed pressure-induced amorphization [21]. In addition, if A1-B_{106} is formed by nonhydrostatic pressure, it transforms to A2-B_{106} at a lower pressure of 81 GPa. It is worth to notice that the β-B_{106} and its induced amorphous phases are metastable phases over 40 GPa compared to the α-Ga phase. The significant structural difference between β-B_{106} and α-Ga phases prevents the continuous phase transition from β-B_{106} to α-Ga under high pressure, which can cause materials to be kinetically trapped in an amorphous phase [21].

People speculated [21] that the B_{12} icosahedra might be stable in the amorphous boron phase over 100 GPa. Recent atom probe experiment and DFT simulations showed that the icosahedra are less stable than the C-B-C chains in B_4C during the field evaporation process [47]. This indicates that the icosahedra are not as strong as people speculate. The present study showed that both the B_{28} cluster and B_{12} icosahedra are deconstructed in the amorphous phase above 81 GPa. No obvious structural changes are observed in A2-B_{106} at ~160 GPa where the superconducting phase appears. It is very likely that the fully amorphous A2-B_{106} phase is the intermediate state between crystalline β-B_{106} and the superconducting phase which might be the α-Ga boron [22]. It is unlikely the icosahedral based β-B_{106} directly transforms to a more close packed α-Ga boron containing no icosahedra. Forming the amorphous phase by fracturing icosahedra seems a rational phase change connecting these two phases.

Recent shock and indentation experiments showed that the abnormal brittle failure of B_4C is related to the amorphous shear band formation under pressure [16,18,41,48]. A lot of efforts have been devoted to explain this abnormal behavior [49–51]. For example, recent DFT [42] and reactive force field (ReaxFF) [52] studies identified the mechanism that the brittle failure arises from the formation of a higher density amorphous band due to the fracture of the icosahedral clusters. For β-B_{106} the failure mechanism under pure shear deformation shows the deconstruction of B_{28} units without fracturing icosahedra. Figure 7(b) showed that both A1-B_{106} and A2-B_{106} have higher density than crystalline β-B_{106}, but lower than α-Ga-B. The average density differences in the whole pressure regime for A1-B_{106} and A2-B_{106} are 2.8% and 9.0%, respectively. This suggests that fracturing B_{12} icosahedra at high pressure likely causes the brittle failure of β-B_{106} and related materials. Consequently, it is crucial to keep the B_{12} icosahedral clusters at high pressure to improve the ductility of β-boron and related materials.

IV. SUMMARY

In summary we used DFT to examine the mechanical properties and shear deformation of β-, τ-, and α-B. We found that the POS in β-B increases the strength and hardness besides stabilizing the structure, while the twins decrease the strength and hardness. The failure mechanism of β-B_{106} is the deconstruction of the B_{28} cluster, while the failure of τ-B_{106} arises from the deconstruction of the B_{28} cluster and nearby icosahedron. Shearing β-B_{106} leads to an amorphous structure (A1-B_{106}) without fracturing the B_{12} icosahedra. The A1-B_{106} transforms to A2-B_{106} amorphous with fully destroyed icosahedra above 81 GPa. This A2-B_{106} phase is

more favorable than crystalline β-B_{106} over 90 GPa, indicating that no icosahedra exist in the amorphous phase over 90 GPa. In addition, the density of A2-B_{106} is 9% higher than β-B_{106}, which suggests that fracturing B_{12} icosahedra under high pressure likely causes brittle failure and fragmentation in β-B_{106} and related materials.

ACKNOWLEDGMENTS

Q.A. was supported by the NRC-HQ-84-15-G-0028 from U.S. Nuclear Regulatory Commission. S.M. was supported by Act 211 Government of the Russian Federation, Contract No. 02.A03.21.0011 and by the Supercomputer Simulation Laboratory of South Ural State University [53].

[1] B. E. Douglas and S.-M. Ho, *Structure and Chemistry of Crystalline Solids* (Springer, Berlin, 2006).
[2] R. E. Hughes, C. H. L. Kennard, D. B. Sullenger, H. A. Weakliem, D. Sands, and J. L. Hoard, J. Am. Chem. Soc. **85**, 361 (1963).
[3] A. R. Oganov *et al.*, Nature (London) **457**, 863 (2009).
[4] N. Uemura, K. Shirai, H. Eckert, and J. Kunstmann, Phys. Rev. B **93**, 104101 (2016).
[5] S.-L. Shang, Y. Wang, R. Arroyave, and Z-K. Liu, Phys. Rev. B **75**, 092101 (2007).
[6] M. A. White, A. B. Cerqueira, C. A. Whitman, M. B. Johnson, and T. Ogitsu, Angew Chem. Int. Ed. **54**, 3626 (2015).
[7] M. J. van Setten, M. A. Uijttewaal, G. A. de Wijs, and R. A. de Groot, J. Am. Chem. Soc. **129**, 2458 (2007).
[8] Q. An, K. M. Reddy, K. Y. Xie, K. J. Hemker, and W. A. Goddard III, Phys. Rev. Lett. **117**, 085501 (2016).
[9] L. V. McCarty, J. S. Kasper, F. H. Horn, B. F. Decker, and A. E. Newkirk, J. Am. Chem. Soc. **80**, 2592 (1958).
[10] D. A. Young, *Phase Diagrams of the Elements* (University of California Press, Berkeley, CA, 1991).
[11] J. L. Hoard and R. E. Hughes, in *The Chemistry of Boron and Its Compounds*, edited by E. L. Muetterties (Wiley, New York, 1967).
[12] B. Albert and H. Hillebrecht, Angew. Chem. Int. Ed. Engl. **48**, 8640 (2009).
[13] T. Ogitsu, E. Schwegler, and G. Galli, Chem. Rev. **113**, 3425 (2013).
[14] H. Zhang, Q. Zhang, J. Tang, and L. C. Qin, J. Am. Chem. Soc. **127**, 2862 (2005).
[15] J. Nagamatsu, N. Nakagawa, T. Muranaka, Y. Zenitani, and J. Akimitsu, Nature (London) **410**, 63 (2001).
[16] V. Domnich, S. Reynaud, R. A. Haber, and M. Chhowalla, J. Am. Ceram. Soc. **94**, 3605 (2011).
[17] G. V. Samsonov, P. Hagenmuller, and T. Lundstrom, in *Boron and Refractory Borides*, edited by V. I. Matkovich (Springer, Berlin, 1977).
[18] M.-W. Chen, J. W. MaCauley, and K. J. Hemker, Science **299**, 1563 (2003).
[19] M. I. Eremets, V. V. Struzhkin, H.-K. Mao, and R. J. Hemley, Science **293**, 272 (2001).
[20] K. Shirai, H. Dekura, Y. Mori, Y. Fujii, H. Hyodo, and K. Kimura, J. Phys. Soc. Jpn. **80**, 084601 (2011)
[21] D. N. Sanz, P. Loubeyre, and M. Mezouar, Phys. Rev. Lett. **89**, 245501 (2002).
[22] U. Häussermann, S. I. Simak, R. Ahuja, and B. Johansson, Phys. Rev. Lett. **90**, 065701 (2003).
[23] B. Siberchicot, Phys. Rev. B **79**, 224101 (2009).
[24] G. Kresse and J. Hafner, Phys. Rev. B **47**, 558 (1993).
[25] G. Kresse and J. Furthmüller, Comput. Mater. Sci. **6**, 15 (1996).
[26] G. Kresse and J. Furthmüller, Phys. Rev. B **54**, 11169 (1996).
[27] G. Kresse and D. Joubert, Phys. Rev. B **59**, 1758 (1999).
[28] Y. Le Page and P. Saxe, Phys. Rev. B **65**, 104104 (2002).
[29] D. Roundy, C. R. Krenn, M. L. Cohen, and J. W. Morris, Phys. Rev. Lett. **82**, 2713 (1999).
[30] J. L. Hoard, D. B. Sullenger, C. H. L. Kennard, and R. E. Hughes, J. Solid State Chem. **1**, 268 (1970).
[31] G. A. Slack, C. I. Hejna, M. F. Garbauskas, and J. S. Kasper, J. Solid State Chem. **76**, 52 (1988).
[32] M. Widom and M. Mihalkovic, Phys. Rev. B **77**, 064113 (2008).
[33] T. Ogitsu, F. Gygi, J. Reed, Y. Motome, E. Schwegler, and G. Galli, J. Am. Chem. Soc. **131**, 1903 (2009).
[34] K. Wade, J. Chem. Soc. D **15**, 792 (1971).
[35] See Supplemental Material at http://link.aps.org/supplemental/10.1103/PhysRevB.95.064108 for the tables listing elastic moduli and the figures for the stress-strain relationships for α-B_{12} and β-B_{106} shearing along the $(001)_r/\langle 100\rangle$ and $(001)_r/\langle \bar{1}00\rangle$ slip system and structural changes as the A1-B_{106} structure is hydrostatic compressed.
[36] R. Hill, Proc. Phys. Soc. A **65**, 349 (1952).
[37] Y.-Z. Ma, C. T. Prewitt, G.-T. Zou, H.-K. Mao, and R. J. Hemley, Phys. Rev. B **67**, 174116 (2003).
[38] R. J. Nelmes, J. S. Loveday, D. R. Allan, J. M. Besson, G. Hamel, P. Grima, and S. Hull, Phys. Rev. B **47**, 7668 (1993).
[39] S. Lee, D. M. Bylander, and L. Kleinman, Phys. Rev. B **45**, 3245 (1992).
[40] X.-Q. Chen, H.-Y. Niu, D.-Z. Li, and Y.-Y. Li, Intermetallics **19**, 1275 (2011).
[41] K. M. Reddy, P. Liu, A. Hirata, T. Fujita, and M.-W. Chen, Nat. Commun. **4**, 2483 (2013).
[42] Q. An, W. A. Goddard III, and T. Cheng, Phys. Rev. Lett. **113**, 095501 (2014).
[43] G. S. Darsavelidze, O. A. Tsagareishvili, T. V. Eterashvili, V. S. Metreveli, G. F. Tavadze, and D. I. Khomeriki, J. Less-Common Met. **117**, 189 (1986).
[44] K. Y. Xie, Q. An, M. F. Toksoy, J. W. McCauley, R. A. Haber, W. A. Goddard III, and K. J. Hemker, Phys. Rev. Lett. **115**, 175501 (2015).
[45] Q. An, K. M. Reddy, J. Qian, K. J. Hemker, M.-W. Chen, and W. A. Goddard III, Nat. Commun. **7**, 11001 (2016)
[46] A. D. Becke and K. E. Edgecombe, J. Chem. Phys. **92**, 5397 (1990).
[47] K. Y. Xie, Q. An, T. Sato, A. J. Breen, S. P. Ringer, W. A. Goddard III, J. M. Cairney, and K. J. Hemker, Proc. Natl. Acad. Sci. USA **113**, 12012 (2016).

[48] V. Domnich, Y. Gogotsi, M. Trenary, and T. Tanaka, Appl. Phys. Lett. **81**, 3783 (2002).
[49] G. Fanchini, J. W. McCauley, and M. Chhowalla, Phys. Rev. Lett. **97**, 035502 (2006).
[50] X. Q. Yan, Z. Tang, L. Zhang, J. J. Guo, C. Q. Jin, Y. Zhang, T. Goto, J. W. McCauley, and M. W. Chen, Phys. Rev. Lett. **102**, 075505 (2009).
[51] D. E. Taylor, J. Am. Ceram. Soc. **98**, 3308 (2015).
[52] Q. An and W. A. Goddard III, Phys. Rev. Lett. **115**, 105501 (2015).
[53] P. S. Kostenetskiy and A.Y. Safonov, *SUSU Supercomputer Resources. Proceedings of the 10th Annual International Scientific Conference on Parallel Computing Technologies* (Arkhangelsk, Russia, 2016).